Real-time tracking of CO migration and binding in the α and β subunits of human hemoglobin via 150-ps time-resolved Laue crystallography

Friedrich Schotte [a], Hyun Sun Cho [a], Jayashree Soman [b], Michael Wulff [c], John S. Olson [b], Philip A. Anfinrud [a,*]

[a] Laboratory of Chemical Physics, National Institute of Diabetes and Digestive and Kidney Diseases, National Institutes of Health, Bethesda, MD 20892-0520, USA
[b] Department of Biochemistry and Cell Biology, and W.M. Keck Center for Computational Biology, Rice University, Houston, TX 77251-1892, USA
[c] European Synchrotron Radiation Facility, BP 220, 38043 Grenoble Cedex, France

ARTICLE INFO

ABSTRACT

We have developed the method of picosecond Laue crystallography and used this capability to probe ligand dynamics in tetrameric R-state hemoglobin (Hb). Time-resolved, 2 Å-resolution electron density maps of photolyzed HbCO reveal the time-dependent population of CO in the binding (A) and primary docking (B) sites of both α and β subunits from 100 ps to 10 μs. The proximity of the B site in the β subunit is about 0.25 Å closer to its A binding site, and its k_{BA} rebinding rate ($\sim$300 μs^{-1}) is six times faster, suggesting distal control of the rebinding dynamics. Geminate rebinding in the β subunit exhibits both prompt and delayed geminate phases. We developed a microscopic model to quantitatively explain the observed kinetics, with three states for the α subunit and four states for the β subunit. This model provides a consistent framework for interpreting rebinding kinetics reported in prior studies of both HbCO and HbO$_2$.

Published by Elsevier B.V.

1. Introduction

In this special issue of Chemical Physics, we honor Prof. Robin Hochstrasser, a man of extraordinary breadth in both experimental and theoretical science, whose pioneering studies have shed much light on many important problems of our time. His enthusiasm and creativity are an inspiration to many, especially to those who have had the privilege to interact with him as graduate students, post-doctoral fellows, or collaborators.

In 1966, when Perutz reported the structure of azide hemoglobin at 5.5 Å resolution [1], he noted that the heme groups to which ligands such as azide can bind were buried deep inside the globin, with amino acid side chains blocking access to the attachment sites. He went on to state, "It is hard to see how the ligand can get past them." Thus, it was clear 47 years ago that a detailed understanding of a protein's function demands characterization of its dynamics as well as its structure. Adult human hemoglobin (HbA) is a tetrameric ligand-binding heme protein comprised of two α and two β subunits (Fig. 1), and continues to serve as an excellent model system for investigating the relations between protein structure, dynamics, and function. The α and β subunits first self assemble into αβ dimers, and then dimerize again to form α1β1/α2β2 tetramers. At the HbA concentration found in blood, the dimer–tetramer equilibrium strongly favors the tetrameric form, which binds oxygen cooperatively and facilitates efficient transport of oxygen from the lungs to the tissues. Ligand binding to a low-affinity T conformational state triggers a structural transition that produces a high-affinity R state. Crystal structures of the liganded (R) and unliganded (T) forms of HbA reveal significant differences in their quaternary conformations and provide a structural basis for understanding cooperative ligand binding. Significantly, the equilibrium between R and T states is not only influenced by the ligation state of its subunits, but also by allosteric effectors and pH, which can fine tune the ligand binding affinity.

A detailed understanding of this complex system requires fundamental knowledge of structural intermediates and their rates of interconversion. Due to α–β heterogeneity, one can enumerate 10 different ligation states for each quaternary conformation. Because the ligand has to migrate between the buried binding site and the surrounding solvent, and may stall along its route, additional states may be required to account for the ligand kinetics. Owing to this complexity, it is not currently possible to solve the complete set of differential equations required to fully describe the function of HbA. Nevertheless, the situation is not without hope, and numerous pioneering studies have helped lay the foundation for investigating hemoglobin with ever more incisive
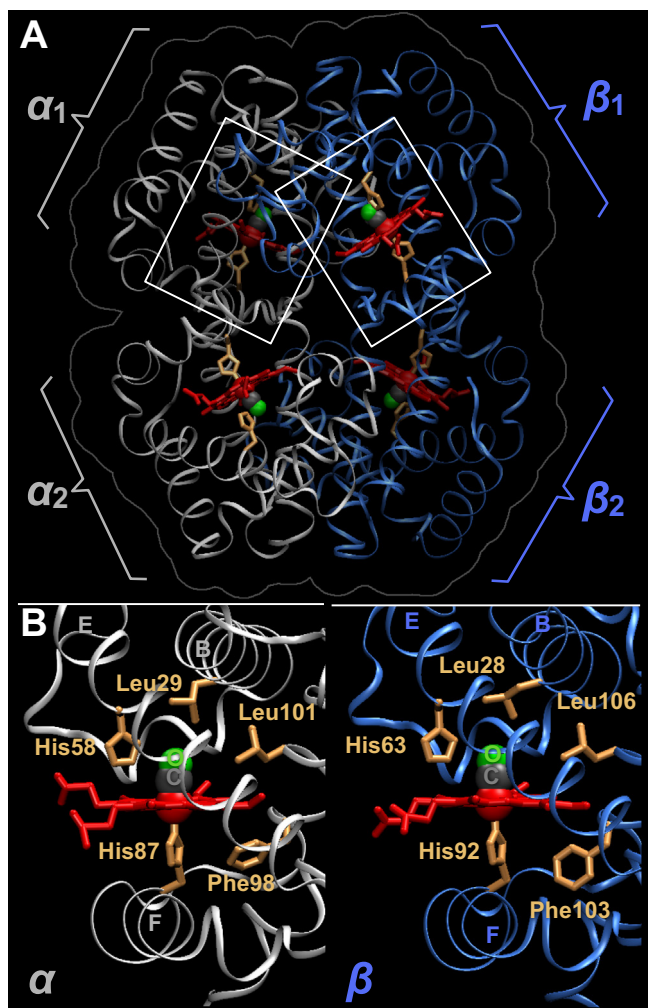
Fig. 1. Structure of carbon-monoxy hemoglobin. (A) HbA tetramer with the heme and adjacent histidines rendered as red and orange sticks, respectively; the heme iron and CO are rendered as spheres; and the α/β subunits are rendered as gray/blue ribbons. The van der Waals surface of the protein is outlined in gray. (B) Enlarged view of the heme region in both α (left) and β (right) subunits. The helices to which key side chains are attached are labeled (B,E,F). Nearby distal and proximal side chains are rendered as orange sticks.

methods. For example, the seminal flash photolysis study by Gibson [2] investigating CO rebinding to HbA with 20 μs time resolution has been extended to nanosecond [3], picosecond [4], and even femtosecond [5] time regimes. In addition, ultrafast time-resolved mid-IR methods focusing on ligand dynamics have been pursued [6–8]. Because these time-resolved methods characterize ensemble averaged behavior, they cannot easily distinguish kinetic differences arising from α–β heterogeneity in native HbA.

Time-resolved Laue crystallography first achieved ~10 ns time resolution in 1996 [9] and was subsequently extended to ~150 ps time resolution [10]. This method is capable of generating near-atomic resolution structures on ultrafast time scales and, therefore, allows real-time visualization of a protein as it functions. Here, we report time-resolved electron density maps of photolyzed HbCO acquired with ~150 ps time resolution. These maps reveal significant α–β differences in the ligand rebinding and escape dynamics. Based upon these kinetic differences, we have developed a new framework for understanding the complex geminate rebinding dynamics observed in this work and prior time-resolved spectroscopic studies.

2. Materials and methods

2.1. Pump–probe method

Time-resolved Laue diffraction 'snapshots' of the photolyzed HbCO structure were acquired on the ID09B beamline at the European Synchrotron and Radiation Facility (ESRF) using the pump–probe method [10] (Fig. 2). Briefly, a laser pulse (pump) photoactivates the crystal, after which a suitably delayed X-ray pulse (probe) passes through the crystal and records its diffraction pattern on a mar135 CCD detector. Because we use a polychromatic X-ray pulse, we capture thousands of reflections in a single image without having to rotate the crystal. This Laue approach to crystallography boosts substantially the rate at which time-resolved diffraction data can be acquired. The information needed to determine the protein's structure is encoded in the relative intensities of the diffraction spots observed. However, the structural information contained in a single diffraction image is incomplete, requiring repeated measurements at multiple crystal orientations to produce a complete set of data.

2.2. Probe pulse (X-ray) generation

Laue diffraction data were acquired when the ESRF operated in 4-bunch mode, in which four 30-nC electron bunches separated by 710 ns circulate in the 6 GeV storage ring. A 2-m long U17 in-vacuum undulator operating at 6-mm gap produced $\sim 10^{10}$ X-ray photons per pulse, which were focused with a toroidal mirror to a 120×80 (H $\times$ V) μm spot at the sample location. The undulator spectrum was peaked at 15 keV with a 5% bandwidth (0.8–1.2 Å FWHM) and included a weak second harmonic feature centered near 30 keV. A high-speed chopper with a 1.7 μs opening window [11] reduced the X-ray pulse repetition frequency to 986 Hz. Single pulses from the 986 Hz pulse train were selected on demand by triggering a millisecond shutter.
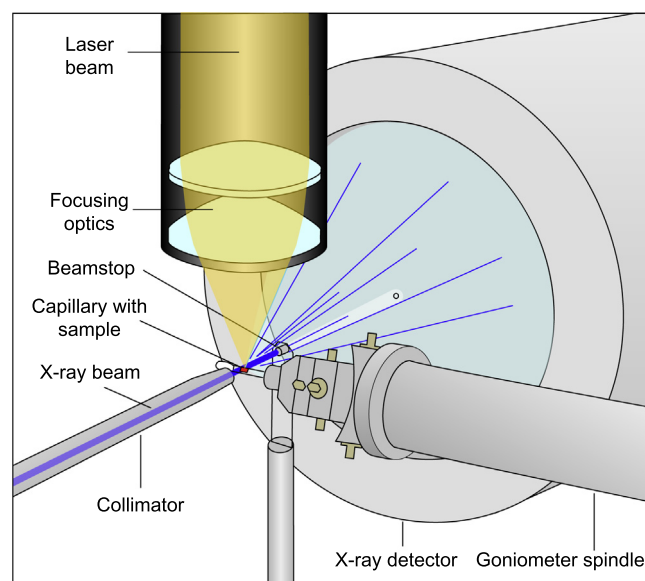

Fig. 2. Pump–probe geometry employed to acquire time-resolved diffraction snapshots. The protein crystal is sealed in a thin-wall glass capillary. Because the laser penetration depth in the crystal is shallow, an orthogonal pump–probe geometry is employed in which the top edge of the protein crystal is positioned at the top edge of the focused X-ray pulse. This geometry ensures optimal overlap between the laser and X-ray illuminated volumes of the crystal. The protein crystal acts as a monochromator and diffracts different X-ray colors in different directions according to Bragg's law. Approximately 2000 diffraction spots are found in each time-resolved diffraction image of hemoglobin.

2.3. Pump pulse (laser) generation

A Coherent Mira laser equipped with Synchro-Lock produced an 88-MHz pulse train (∼100 fs; 780 nm) that was phase locked to the 4th subharmonic of the 352 MHz ring RF. These pulses seeded a Spectra Physics Hurricane regenerative amplifier, which produced ∼1 mJ, 780 nm pulses at 986 Hz, the same frequency as the high-speed X-ray chopper. These pulses pumped a Light Conversion TO-PAS, which generated ∼100 fs, 62 µJ, 520 nm pulses. The pulses were stretched, and the beam profile homogenized by focusing the laser pulses in a 200-µm, multimode optical fiber. Nonlinear processes in the fiber shifted and broadened the optical spectrum to span the range 500–560 nm. An optical relay lens assembly equipped with a cylindrical lens focused the fiber output to an elliptical spot at the sample location. A pulse energy of 42 µJ focused to $90 \times 250\,\mu m$ (FWHM) produced an energy density of ∼2 mJ/mm². The timing electronics controlling the laser pulse amplification were triggered to produce pump pulses on demand. The coarse timing between the laser and X-ray pulse arrival was controlled by Stanford Research Systems DG535 delay generators, whereas fine control was achieved with a calibrated, voltage-controlled RF phase shifter inserted between the Synchro-Lock and the laser oscillator. To monitor the pump and probe arrival times, a neutron-irradiated GaAs photoconductor that is sensitive to both laser and X-ray pulses was positioned at the sample position. A 3-GHz Tektronix TDS 694 digital oscilloscope monitored the two pulses and was used to define the delay settings required to achieve coincidence. A combination of computer-controlled digital delay and phase shifter delay settings were used to set the pump–probe delay to the targeted value.

2.4. Sample preparation

Human hemoglobin A crystals were grown according to the protocol of Perutz [12] in sealed tubes under 1-atm CO from solutions containing 15 mg/ml protein, 2.2–2.5 M sodium/potassium phosphate, pH 6.8 and a small amount of toluene. This method produced large (∼250 µm), high quality, bi-pyramid shaped HbCO crystals that belong to space group P4₁2₁2. Crystals selected for time-resolved experiments were transferred into CO-purged 1-mm diameter quartz glass X-ray capillaries. After wicking out excess mother liquor surrounding the crystal, the capillary was pressurized to ∼4 atm CO and sealed with UV-cure epoxy.

2.5. Data collection protocol

The HbCO crystals were first manually centered at the intersection of the laser and X-ray beams using a Huber goniometer head. An orthogonal pump–probe geometry was employed, in which the crystals were photolyzed by a laser pulse focused on the top face of the crystal. To ensure the X-ray beam probes the photolyzed por-tion of the crystal, we scanned the crystal vertically through an attenuated X-ray beam and recorded its diffraction pattern as function of position. We analyzed the diffraction strength to find the position where the 80 µm X-ray beam (vertical dimension) was centered 40 µm below the top edge of the crystal. With this approach, the X-ray beam probed the crystal to a depth of ∼80 µm.

An Oxford cryo-cooling stream chilled the crystal to 15 °C during data acquisition. Images were read out after accumulating from 8 to 32 X-ray shots at 3.3 Hz. A complete time series was acquired sequentially at the same crystal position before rotating to the next angular setting. Data sets were acquired with up to 72 angular settings per crystal spanning ±90° with 2.5° spacing. The sample to detector distance was 125 mm for three crystals and 140 mm for one crystal. Data from four different HbCO crystals were merged (Table 1). A reference image for each time series was acquired by setting the pump–probe time delay to −10 ns.

2.6. Data analysis

The Laue diffraction images were indexed with TReX and integrated with PRoW [13]. The integrated spot intensities were wavelength normalized with LSCALE [14], and redundant observations at each time point were scaled and merged with SCALA [15]. Electron density maps for the ground and photolyzed states were generated using SIGMAA and Bourgeois [16] weighting.

The level of photolysis achieved in this study was estimated from the 100 ps maps by visual assessment. Briefly, we generated a series of extrapolated electron density maps with the assumed photolysis level incremented in steps of 0.05. When set to 0.15, the electron density distribution of CO in the primary docking sites of both α and β subunits appeared to be uncontaminated by electron density from the binding site. As expected, the photolysis levels in the α and β subunits were found to be the same.

The CO population found in a particular site was determined by integrating the electron density within a 1.0 Å radius sphere centered on that site. With a sphere of this size, we sample ∼6 of the 14 electrons in CO. Since X-ray diffraction data can be put on an absolute scale, the number of electrons found in a given site can be converted to fractional occupancy of CO.

Due to overlap of the red and blue circles in Fig. 4, our integrated electron density determination suffers from 'cross talk' between the binding site (A) and primary docking site (B). For example, loss of electron density in A is partially offset by a gain of electron density in B. We corrected for cross talk using the equations:

$$q'_A = \frac{q_A - c \cdot q_B}{1 - c^2}$$

$$q'_B = \frac{q_B - c \cdot q_A}{1 - c^2}$$

where q_A (q_B) represents the integrated number of electrons found in the A (B) site, and c quantifies the cross talk between the two integration spheres. The absolute scale and the cross-talk terms are set so that the loss of electrons in the A binding site is normalized to one CO molecule, and the CO population in the B site of the β subunit goes to zero at long times.

Our estimation of the photolysis branching fraction, ϕ_B, is based on the corrected integrated electron densities found in the A and B sites at 100 ps (Fig. 4). If 100% of the CO ends up in the B site ($\phi_B = 1$), the electron density change in the B site will be equal to and opposite that in the A site. If the CO electron density spills beyond the integration sphere, or if some CO is diverted elsewhere, the photolysis branching fraction will be less than 1. To distinguish between these possibilities, we repeated our determination with a larger integration sphere. Since the 'missing' population in the B

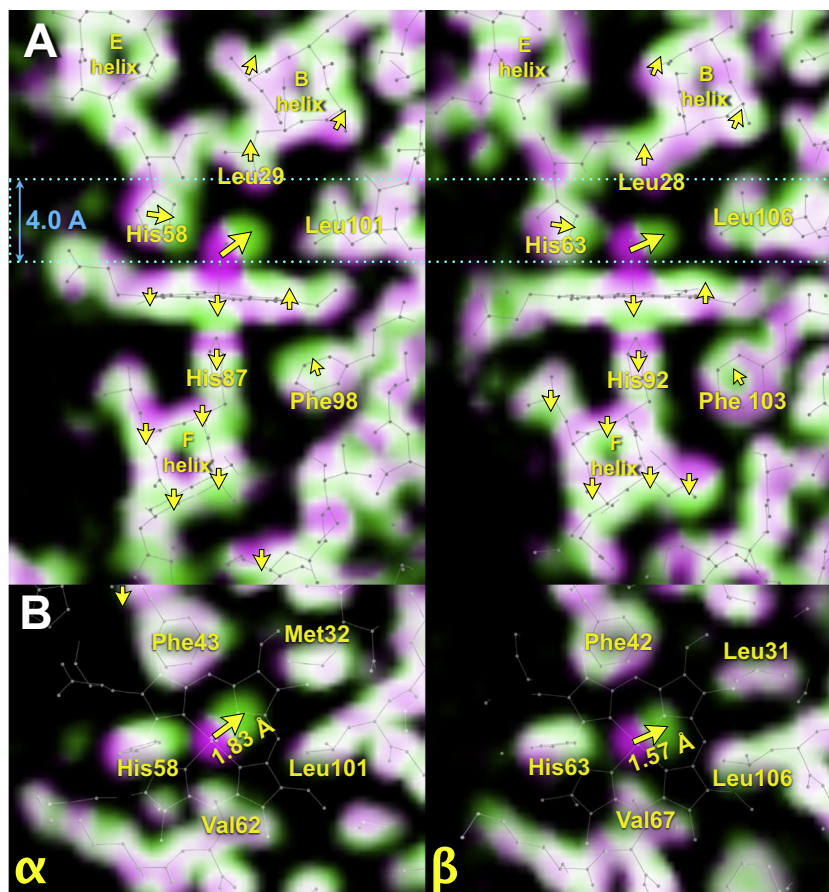|	
Unit cell a, b, c [Å]	54.016, 54.016, 194.794
Unit cell α, β, γ [°]	90, 90, 90
Spacegroup	P4₁2₁2
Wavelength range [Å]	0.8–1.2
d_{min}	2.0 Å
No. of reflections	818,961
Unique reflections	19,739
Unique reflections (I/σ > 2)	16,371
Redundancy	41.1 (33.7)
<I/σ>	18.7 (3.5)
Completeness (I/σ > 2)	79.7% (50%)

Fig. 3. Time-resolved electron density maps of α and β subunits acquired at 100 ps. The ground state electron density maps are colored magenta, and the time-resolved maps are colored green. Where magenta and green overlap, the electron density blends to white. The magenta-to-green color gradient indicates the direction of atomic motion (yellow arrows). For clarity, some side chains have been omitted. The stick models correspond to refined ground state structures. (A) Side view. (B) Top view of the heme region. The arrows indicate the magnitude of the CO center-of-mass displacement, which was estimated from the centroid in the electron density distribution. The slabbing depth for this view corresponds to the cyan box in panel A.

site decreased only modestly (∼5%) when doubling the volume of the integration sphere (by increasing its radius from 1.0 to 1.26 Å), we conclude that most of the missing CO was diverted elsewhere.

Error estimates for the integrated electron density were obtained by integrating three sites in the solvent region of the unit cell with a sphere of the same radius, and calculating the root-mean-squared deviation of the electron count across the time series. This approach established a noise floor of ∼0.24 electrons rms, which corresponds to uncertainty in the CO occupancy of ±4%.

3. Results and discussion

3.1. Time-resolved electron density maps

Time-resolved snapshots of the HbA structure were acquired from 100 ps to 10 μs with one time point per decade. The 100-ps electron density maps for α and β subunits are shown in Fig. 3, which provides two orthogonal views of the region surrounding the heme. The HbA maps reveal numerous features in common with those found in prior studies of myoglobin [17]. Upon photolysis, CO vacates the heme binding site and takes up residence in a nearby primary docking site (see yellow arrows in Fig. 3B); the distal histidine swings toward the vacancy created by CO translocation; and the heme iron moves downward and out of the heme plane. Correlated motions involving other parts of the protein are

indicated with yellow arrows. Electron density maps constructed from half of the time points acquired (100 ps, 10 ns, and 1 μs) are shown in Fig. 4, which focuses on the vicinity of the heme and identifies with colored circles sites in which CO can be found. It is clear from Fig. 4 that CO escapes from the primary docking site of β subunits far faster than it does from α subunits (see blue circles). Indeed, absence of CO at 10 ns implies that its lifetime in this site is at most a few ns. Geminate recombination from this site is too fast to be resolved in most prior time-resolved spectroscopic studies of ligand rebinding dynamics in HbA, which typically reported time resolution no better than 5–10 ns.

Due to crystal constraints, the cooperative R to T structure transition cannot be accommodated in the crystal. Indeed, the strain induced by this transition can crack the crystal. Since the level of photolysis is relatively low and the geminate rebinding yield high (see Section 3.2 *Time-resolved, site-specific CO population*) the persistent strain is minimal and the crystals survive repeated photolysis. The dynamics reported here were recorded before the ∼20 μs time scale for the R to T structure transition [3], and therefore correspond exclusively to ligand migration and rebinding dynamics in the high-affinity R state of HbA.

3.2. Time-resolved, site-specific CO population

The ability to put crystallographic observations on an absolute scale is unique among time-resolved methods. Indeed, the inte-
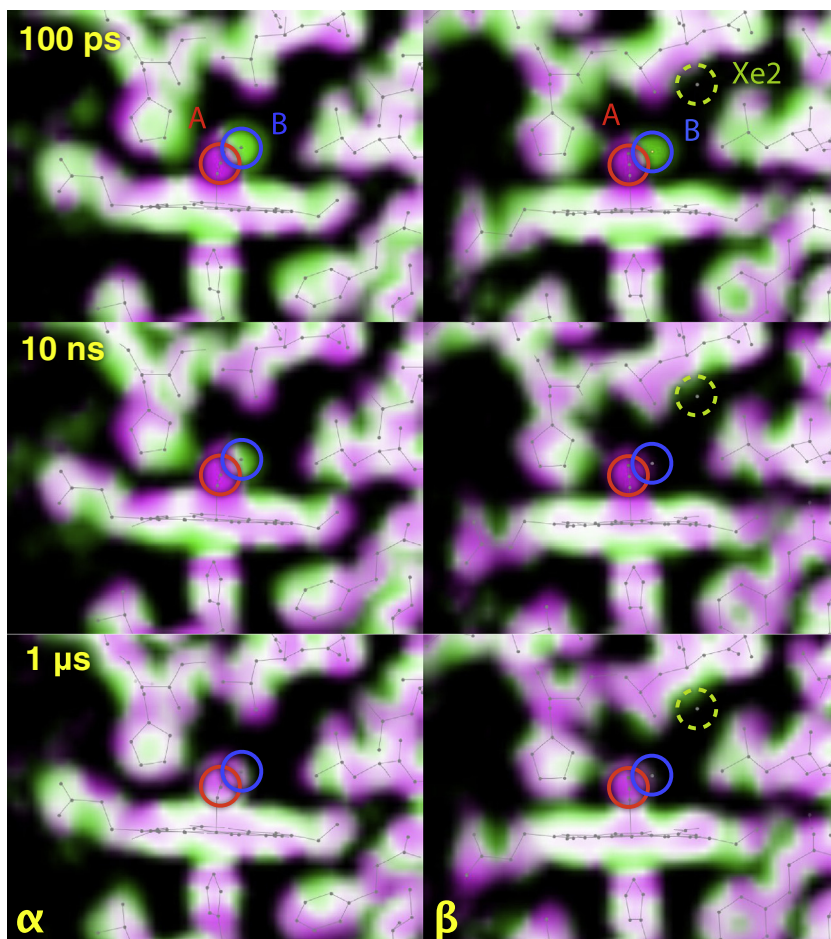
Fig. 4. Time-resolved electron density maps of α and β subunits acquired at 100 ps, 10 ns, and 1 μs. The color-coding scheme is the same as in Fig. 3. The colored circles indicate sites where CO is observed in this study: heme binding site (A; red) and primary docking site (B; blue). The dashed circle labeled Xe2 in β identifies an internal cavity into which Xe can diffuse in T-state HbA [18], and CO can be found following continuous photolysis of T-state HbCO under cryogenic conditions [19]. For clarity, some side chains have been omitted. The stick models correspond to refined ground state structures.
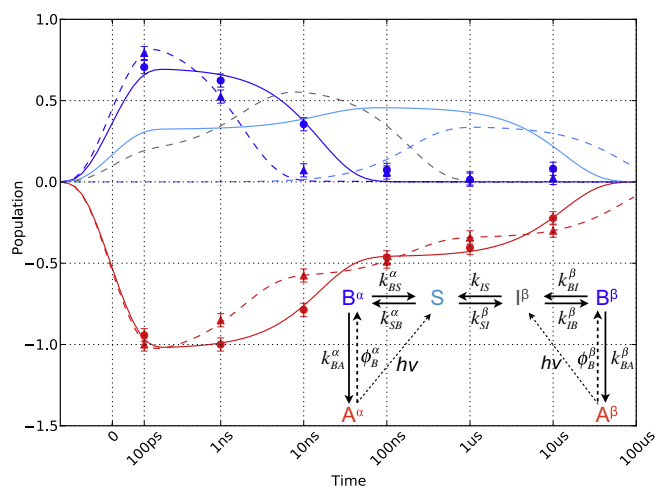

Fig. 5. Time-dependent population of CO found in A and B sites of α (filled circles) and β (filled triangles). The modeled populations of A (red), B (blue), I (gray) and S (cyan) are plotted as solid (α subunits) and dashed (β subunits) lines, and are well described by the parameters in Table 2.

grated electron density in each of the sites indicated in Fig. 4 can be translated into its CO occupancy, for which 14 electrons corresponds to an occupancy of 1. Exploiting this capability, we have

quantified the time-dependent CO population in each of these sites and have charted the results in Fig. 5. The measured populations have been divided by the photolysis yield (0.15), which extrapolates the data to 100% photolysis. To properly calibrate these measurements, it is crucial to capture a snapshot before the ligand can escape from the primary docking site or rebind to the heme. The time resolution achieved in this study, ~150 ps, proved sufficient for this calibration.

3.3. Xenon binding sites

In myoglobin (Mb), four internal cavities have been shown to accommodate Xe under pressure [20], with two of those sites, Xe1 and Xe4, transiently occupied by CO after photolysis of MbCO [10,17,21–23]. In T-state deoxy HbA, five internal cavities have been shown to accommodate Xe under pressure, two of which are found in the β subunit [18]. The Xe2 site in β is located within 1 Å of the Xe4 site found in Mb [18], and is indicated as a dashed circle in Fig. 4. In spite of its similarity to the Xe4 site in Mb, we find no convincing evidence for CO sequestration in this site nor any other nearby location in either subunit.

Adachi et al. [19] reported crystal structures of T-state cross-linked iron–nickel hybrid hemoglobins, XL[α(Fe–CO)–β(Ni)]$_2$ and XL[α(Ni)–β(Fe–CO)]$_2$, both before and after photolysis at 25 K. Their difference maps showed CO trapped in one location in the α subunit, but two locations in the β subunit with a small

population found in the Xe2 site. However, when they photolyzed R-state HbCO, they found no evidence for CO migration into the Xe2 site, in agreement with our result.

In contrast to MbCO, Xe binding sites appear to play a minimal role in R-state HbCO. This conclusion is consistent with the observation that ligand recombination in HbA is minimally affected when pressurized with 9 atm Xe [24].

3.4. Kinetic model

A complete description of the ligand rebinding dynamics in HbA requires knowledge of all states involved. States that cannot be observed directly with time-resolved crystallography have to be inferred from the observed kinetics and modeled accordingly. The time-dependent populations of CO in Fig. 5 reveal significant kinetic differences between the α and β subunits. The rebinding kinetics in the β subunits are more complex and require a four-state model to reproduce the time-dependent populations of the intermediates (see inset in Fig. 5). In contrast, the rebinding dynamics in the α subunits are reproduced with a simpler 3-state reaction scheme.

The CO rebinding kinetics in the α subunit is biphasic, with the first phase corresponding to geminate rebinding and the second presumably corresponding to bimolecular rebinding of CO from the solvent. Thus, the ligand dynamics can be reproduced with a simple three-state model involving A, B, and presumably S (CO in the solvent). Indeed, the experimentally determined A- and B-site populations are reproduced with high fidelity using the kinetic parameters in Table 2.

The CO rebinding kinetics in the β subunit has three phases. Upon photolysis, CO translocates from its binding site, A, to a primary docking site, B. From B, CO can either rebind to A or migrate to other sites in or around the protein. To visualize and quantify CO in sites other than A and B, the population in these locations must be sufficient to rise above the noise level. Since no other sites are observed, CO that has escaped from B must become delocalized in or around the protein. We group these delocalized sites collectively into an intermediate state denoted "I". Once CO accesses the protein-water interface, it either becomes solvated, S, or migrates back into the protein, possibly returning to B and rebinding in a delayed geminate phase. Once solvated, CO rebinds bimolecularly on a much longer time scale with second order kinetics.

About 43% of the CO rebinding amplitude in the β subunits (red triangles) occurs in less than 10 ns and terminates when CO escapes from the primary docking site (blue triangles). This prompt geminate phase follows first order kinetics. If the escaped CO were to promptly disappear into the surrounding solvent, S, the next rebinding phase would be bimolecular and would follow second order kinetics. Instead, we observe a second rebinding phase that is somewhat smaller in amplitude than the first. Because it occurs on the 100 ns time scale, it is far too fast to be bimolecular and must therefore be a second, delayed geminate phase. Evidently, CO migrates from B^β to I^β, from which it can return to B^β and rebind in a delayed geminate phase. The delayed geminate phase is arrested when CO escapes from I^β into the surrounding solvent, S, after which CO rebinding enters its third and final phase, which is bimolecular.

Where might I^β be located? We favor the following possibility: I^β corresponds to CO delocalized at the protein-solvent interface on the left side of the distal histidine (Figs. 3 and 4), which is a short distance from B^β. Migration into the surrounding solvent from I^β involves solvating an apolar molecule, for which there is an enthalpic barrier. Therefore, it would not be surprising for CO to shuttle back and forth between I^β and B^β before its fate is ultimately determined: it will either rebind to the heme iron via B^β or overcome the barrier to solvation and become S. This view is consistent with recent MD simulations involving R-state β subunits [25], where the dominant (95%) pathway for CO migration was around the distal histidine and to the protein-solvent interface.

The information embodied in the time-dependent A- and B-site populations in β subunits is sufficient to refine all corresponding parameters in the four-state model shown in Fig. 5, which reproduces the population dynamics with high fidelity using the parameters in Table 2. Note that the instrument response function, which corresponds to the convolution of the laser pump and X-ray probe pulses, was accounted for when modeling the time-dependent populations.

The uncertainties in Table 2 represent the precision of our rate determination, and were computed from the co-variance matrix returned from the non-linear least-squares Levenberg–Marquardt fit of the data. The accuracy of the rate constants is limited by both the signal-to-noise ratio of the data and the sparsity of the time points (one per decade).

3.5. Photolysis branching fraction

Our kinetic model includes a photolysis branching fraction parameter, ϕ_B, which represents the probability that photolyzed ligands appear in the B site. This parameter accounts for the fact that protein structure fluctuations can transiently gate ligand access to locations other than the B site [26]. According to Table 2, most of the photolyzed CO appears in the B sites ($\phi_B = \sim 0.75$). If the electron density of CO spreads beyond our integration sphere, our determination of ϕ_B will underestimate the yield. As discussed in Section 3.8. *Relevance to O_2 binding*, the geminate yield reported in HbO_2 studies requires ϕ_B to be less than 1.0. Therefore, its true value must be between ~ 0.75 and 1.0. The fact that most of the dissociated CO can be found inside a 1.0 Å radius sphere centered on the B site suggests that CO is tightly constrained in this site by the surrounding side chains. Indeed, it has been suggested that CO may be stabilized in the B site by a weak hydrogen bond with the distal histidine [27]. This localized interaction would help keep the probability distribution of CO from spreading over the full spatial extent of an L-shaped distal cavity described in early MD simulations of Mb [28].

3.6. Evidence for distal control of ligand dynamics

By quantifying the time-dependent population of CO in its binding site (A) and nearby primary docking site (B), we can determine unambiguously the elementary rate constants for ligand binding and escape from the B site. In spite of their structural similarity (see Fig. 3), the α and β subunits of HbA exhibit significantly

Table 2
Refined parameters used to model the time-resolved populations of A and B in Fig. 5. Also tabulated are ϕ_{gem}, the geminate rebinding yield, and d_{A-B}, the CO center-of-mass displacement when translocating from A to B.

	α	β
φ_B	0.68 ± 0.04	0.83 ± 0.05
k_{BA} [μs^{-1}]	51 ± 10	300 ± 70
k_{BS} [μs^{-1}]	12 ± 6	–
k_{SB} [μs^{-1}]	0.09 ± 0.03	–
k_{BI} [μs^{-1}]	–	240 ± 80
k_{IB} [μs^{-1}]	–	4 ± 4
k_{IS} [μs^{-1}]	–	3 ± 3
k_{SI} [μs^{-1}]	–	0.03 ± 0.06
φ_{gem}[a]	0.54	0.66 (0.43 + 0.23)
d_{A-B} [Å][b]	1.83, 1.86, 1.95	1.57, 1.60, –

[a] Values in parenthesis indicate contributions from the prompt and delayed phases.
[b] Displacements determined from 100-ps, 1-ns, and 10-ns (α only) maps.

different rates. For example, the rebinding rate with CO localized in the B site (k_{BA}), was found to be ~6 times faster in the β subunits.

The ligand displacement when translocating from A to B was determined for all frames in which CO is visible (Table 2). The d_{A-B} displacement in the α subunit is ~1.83 Å at 100 ps, and increases to ~1.95 Å by 10 ns. Evidently, conformational relaxation of the protein following photolysis pushes CO farther from the heme iron and should slow the rate of geminate recombination. However, our time-resolved data points are too sparse to detect, much less quantify, a time-varying rate coefficient for the prompt geminate rebinding phase. Intriguingly, the d_{A-B} ligand displacement in the β subunit is ~0.25 Å smaller than that observed in the α subunit, and its k_{BA} rate is 6-fold faster. The fact that a ~0.25 Å displacement can modulate the k_{BA} rebinding rate by a factor of 6 illustrates the remarkable sensitivity of this rate to small structural changes. This correlation provides evidence for distal control of the geminate rebinding rates.

Adachi and coworkers reported cryo-crystallography structures of hybrid T-state HbCO determined before and after photolysis in frozen crystals held at 25 K. From those structures, we calculated the center-of-mass distances between bound and 'docked' CO in both α (1.62 Å) and β (1.76 Å) subunits. The displacements found in our study at 100 ps for R-state α (~1.83 Å) and β (~1.57 Å) subunits are similar in magnitude but reversed. (Although that study also investigated R-state HbA under cryogenic conditions, they didn't report coordinates for those structures, so we are unable to make a direct comparison between our respective R-state results.)

What is the structural basis for modulating the k_{BA} rates in R state HbA? The side chains circumscribing the distal pocket are the same except for one: upon photolysis, CO moves toward Met32 in the α subunit and toward Leu31 in the β subunit (Fig. 3B). Since the side chain in Met32 is linear whereas Leu31 is branched (both have the same number of heavy atoms), one might expect the linear side chain to have greater packing flexibility, and may allow CO to move further from the A site. Indeed, the Met32 motion in the α subunit in Fig. 3B is correlated with that of the distal histidine and the CO, and facilitates a larger displacement away from the binding site compared to the β subunit, where the Leu31 motion appears to oppose the CO displacement.

The structure of the protein circumscribing the distal cavity also affects the rate of ligand escape from the B site, which was found to be ~20 times faster in the β subunits (k_{BI} vs. k_{BS}). Fig. 3 provides a clue regarding the structural origins for this difference: the heme propionate is oriented downward in the β subunit, whereas it is oriented upward in the α subunit, and is stabilized in this position by a hydrogen bond between its carboxylate oxygen and nearby His45 [29]. Closer proximity of the propionate to the distal histidine in the α subunit may constrain the histidine motion, and slow the rate at which the ligand can slip by the distal histidine and access the protein-solvent interface. Note that an upward propionate orientation is also found in MbCO, whose B site residence time [17] is significantly longer than that found in the β subunit of HbA.

3.7. Comparison with prior work

With time-resolved Laue crystallography, the α and β subunits can be characterized independently within intact, tetrameric HbCO crystals. In contrast, time-resolved spectroscopic studies of HbCO in solution record ensemble averaged signals that typically lack the specificity required to distinguish between α and β subunits. To overcome this limitation, spectroscopic studies have characterized subunit-specific kinetics using isolated α and β subunits [24,30], or hybrid HbA tetramers in which one of the subunits contains a different metal-porphyrin complex [31,32] or a mutated active site [24]. We should exercise caution when comparing our

results with dynamics recorded in isolated subunits, as isolated chains are not necessarily isolated: purified β subunits undergo concentration-dependent self assembly into dimers and tetramers [33]. Moreover, the CO rebinding rate in the $β_4$ tetramer was reported to be ~2.5 times faster than in the dimer [33].

A picosecond time-resolved study of isolated β subunits in 75% glycerol-water reported CO rebinding dynamics over a large temperature range spanning 40 to 300 K [34]. At 300 K, the rate extracted for k_{BA} (330 μs^{-1}) is similar to that reported here (300 μs^{-1}), and confirms the presence of a fast geminate rebinding phase in β subunits. The agreement is surprisingly good considering differences in sample preparation (isolated β subunits in 75% glycerol vs. intact, tetrameric HbCO crystals), and considering the difficulty extracting rate constants from a highly complex, nonexponential rebinding curve [34].

Time-resolved spectroscopic studies of α(Fe–CO)β(Co) and α(Co)β(Fe–CO) HbA hybrids allowed subunit-specific assessment of CO rebinding dynamics in both R- and T-state HbA. The geminate rebinding rate in R-state α subunits (26 μs^{-1}) [32] was found to be twice the rate in β subunits (13 μs^{-1}) [31]; the geminate yield for α and β was reported to be the same. Similar geminate recombination rates for wild-type α subunits (34 μs^{-1}) and β subunits (10 μs^{-1}) in mutant hybrids were reported [24]. Since these time-resolved spectroscopic studies were performed using ~7–10 ns laser pulses, the rates determined for the β subunits corresponds to the delayed, not the prompt geminate phase. The range of rates ascribed to prompt geminate rebinding in the α subunit (26–34 μs^{-1}) are approximately half our observed rate (63 μs^{-1}). The range of rates ascribed to the delayed geminate phase in the β subunit (10–13 μs^{-1}) is approximately twice our observed rate ($k_{IS} + k_{IB} \cdot k_{BA}/(k_{BA} + k_{BI}) = $ ~5 μs^{-1}). The differences observed are likely due to crystal packing effects, which constrain conformational motion of the protein. In the α subunit, hindered side chain motion keeps CO in closer proximity to the binding site and accelerates its prompt geminate rebinding phase. The delayed geminate phase in the β subunit is slowed by hindered ligand migration between I and B.

In this study, the bimolecular rebinding phase appears sooner than observed elsewhere, and is due to differences in the CO concentration present in the surrounding solvent. In most time-resolved spectroscopic experiments, the HbA concentration is low compared to the CO concentration in solution (~1 mM at 1 atm CO). Consequently, photolysis minimally alters the CO concentration in solution, and the bimolecular rebinding phase is pseudo first order with ~1 mM CO. The situation is quite different in HbCO crystals, whose heme concentration is 49 mM. At 15% photolysis, and with approximately 40% of the dissociated CO escaping into the surrounding solvent, the CO concentration in solution is boosted the equivalent of 2.8 atm CO pressure. Since we pressurized the capillary to ~4 atm CO, the bimolecular CO binding rate should start out ~6.8 times faster than that observed in studies conducted at 1 atm CO pressure, and should end ~4 times faster. We observe this expected acceleration, but also find that the bimolecular phase in the α subunit seems to be significantly faster than that observed in the β subunit. It is possible that a delayed geminate phase exists for α subunits as well, though we cannot see this phase clearly, due in part to sparseness in the time points and lack of data beyond 10 μs. Indeed, recent MD simulations involving R-state α subunits [25] suggest that only a small fraction of the photolyzed CO escapes from $B^α$ to the protein-solvent interface via the distal histidine pathway (7.5%); most of the time, CO explores multiple pathways that penetrate into the protein interior. It is possible that we are witnessing the return of CO from more remote regions in the protein interior, which would be expected to take longer than the time required for CO return in the β subunit, where the putative I state is near the B site.

3.8. Relevance to O_2 binding

Hemoglobin is designed to transport O_2, not CO. Because O_2 rebinds to the heme more rapidly and more efficiently than CO, time-resolved studies of HbO_2 require both higher time resolution and higher sensitivity to track the relatively small population of deoxy HbA that survives beyond the prompt geminate rebinding phase. Under the *in vitro* conditions typically used in time-resolved studies of HbO_2, the heme undergoes auto-oxidation [35], which degrades the HbA sample and further complicates interpretation of the data. Thus, most studies of ligand dynamics in HbA have used CO as a surrogate for O_2, and their authors have made the argument that the results obtained are relevant to HbO_2. The predictive capabilities of the microscopic model presented in this study suggest that this argument is justified.

A picosecond time-resolved study of photolyzed tetrameric HbO_2 [36] reported biexponential geminate rebinding in which 25% of the photolyzed population rebinds with a 0.14 ± 0.02 ns time constant (~7000 μs^{-1}), 49% with a 0.98 ± 0.12 ns time constant (~1000 μs^{-1}), and $26 \pm 3\%$ persists to longer times. Approximately half the persisting population rebinds in a delayed geminate phase with a time constant averaging 33.5 ± 2 ns (~30 μs^{-1}) over a range of pH spanning 6.1 to 8.5 [37]. Our 4-state model provides a framework for assigning these rates to specific processes in specific subunits.

Due to their similarity in size and dipole moment, we expect the rate of O_2 and CO escape from (and return to) the B sites to be similar. On the other hand, O_2 is far more reactive with the heme iron. Indeed, its ultrafast geminate rebinding rate (~7000 μs^{-1}) is ~23 times faster than k_{BA} for CO in the β subunits of HbA (~300 μs^{-1}). The heightened O_2 reactivity is due in part to differences in binding geometry: since CO binds upright [38,39] with the C end covalently linked to the heme iron, whereas O_2 binds at an angle from either end [39], O_2 enjoys a significantly larger capture cross section for rebinding from the nearby B site. If distal control of the k_{BA} rate is achieved by regulating ligand proximity, as suggested by our HbCO study, then it should be operative for both O_2 and CO. Interestingly, the faster of the two prompt geminate phases in HbO_2 is 7 times faster, which is similar to the 6 times faster rate by which CO rebinds to β vs. α subunits in photolyzed HbCO crystals. If the difference in the relative CO and O_2 rebinding rates were dominated by differences in their capture cross section, it would not be unreasonable to associate the faster biexponential O_2 rebinding rate to β subunits (~7000 μs^{-1}), and the slower one to α subunits (~1000 μs^{-1}).

The implications of this assignment, which differs from that proposed by Dzhagarov and coworkers [36], are far reaching. Since the k_{BA} O_2 rebinding rates are fast compared to the corresponding ligand escape rates in β (240 μs^{-1}) and α subunits (12 μs^{-1}), only a small fraction of O_2 in the B sites manages to escape. Indeed, in the limit $\phi_B = 1.0$, the escaped fraction sums to a maximum of $\sim2\%$ of the total photolyzed population. Since this amplitude is small compared to the 26% amplitude for the persisting deoxy population [37], the delayed geminate rebinding phase necessarily involves ligands that bypassed the B sites during photolysis, i.e., ϕ_B is less than 1.0. Since the α subunit accounts for half of all hemes, and therefore half of the photolyzed O_2, its 49% geminate amplitude implies that 98% of the O_2 in the α subunit rebinds from its B site. Thus, the α subunit contributes negligibly to the delayed geminate and bimolecular phases. Assigning the 25% geminate rebinding amplitude to the β subunit implies that its photolysis branching ratio is about 0.5, i.e., 50% of the photolyzed O_2 appears in the B site, and 50% appears in the I state. The population in I represents 25% of the total, and is comparable to the persisting population observed after the prompt geminate phases terminate. Accordingly, the delayed geminate phase corresponds to O_2 migrating from the I state

to the B site in the β subunit, whereupon it rapidly rebinds. Approximately half rebinds and half escapes into the surrounding solvent, and accounts for the $\sim13\%$ bimolecular rebinding amplitude observed at much longer times.

According to our rate assignments, the delayed geminate rebinding rate (~30 μs^{-1}) corresponds to the rate of ligand migration rate from I to B. When CO migrates from I to the B site in the β subunit, it rebinds with a probability $k_{BA}/(k_{BA} + k_{BI})$, which according to our study is 0.46. Therefore, the delayed geminate phase for CO rebinding in the β subunits of HbA should be slower than that for O_2, and should have a rate of $0.46 \cdot 30$ μs^{-1} = 13.8 μs^{-1}. This prediction is in excellent agreement with the CO geminate rebinding rate of 13.2 μs^{-1} reported for β subunits in R-state α(Co)β(Fe–CO) hybrid Hb [31]. The accuracy of this prediction provides further support for our model and our assignment of the ~30 μs^{-1} geminate phase of O_2 binding to ligand migration from I to B in β subunits.

Is a $\phi_B = 0.5$ photolysis branching fraction for the β subunits of photolyzed HbO_2 plausible, as required by our rate assignments? For comparison, the photolysis branching fraction assigned to the β subunits of photolyzed HbCO is $\phi_B = 0.83$. Due to differences in their binding geometry, ϕ_B in HbO_2 need not be the same as what we determine for HbCO. For example, the O_2 in HbO_2 forms a strong hydrogen bond with the distal histidine [29], and its relative orientation compared to upright CO should influence its photolysis branching fraction. Moreover, the impulsive half-collision that ensues during photolysis of ligands bound in a linear vs. bent configuration would partition kinetic energy unequally into their respective rotational and translational degrees of freedom [6], and could also influence the O_2 vs. CO photolysis branching fraction. The likelihood of the photolysis branching fraction being different for O_2 and CO is a target that could be explored further with MD simulations.

4. Conclusions

Measurement of the time-dependent CO population in the A and B sites of both α and β subunits has led to a microscopic model for ligand rebinding in tetrameric HbCO that not only rationalizes our time-resolved crystallographic observations, but also provides an experimentally defensible framework for reconciling the similarities and differences observed in prior studies of CO and O_2 rebinding dynamics in HbA.

In contrast to MbCO, Xe binding sites appear to play a minimal role in R-state HbA, as we find no evidence for CO sequestration in any of the reported Xe sites. The prompt geminate rebinding rate in β subunits was found to be 6 times faster than in α, and is too fast to be observed in most previous time resolved studies. The relative k_{BA} rates for the α and β subunits are correlated with CO displacement from the heme binding site, and provides evidence for distal control of the geminate rebinding rate. Our four-state model for β subunits includes an 'I' state to account for the delayed geminate phase. Moreover, we introduce a photolysis branching fraction, which recognizes that most but not all dissociated CO appears in the B site. The framework provided by this model allows assignment of geminate rates observed in photolyzed HbO_2 to specific subunits, and helps reconcile observations reported in spectroscopic studies of CO vs. O_2 rebinding dynamics. Indeed, our microscopic model for geminate rebinding of CO to HbA reproduces the O_2 rebinding dynamics by simply increasing the elementary rebinding rate k_{BA} in both α and β subunits by a factor of 23, keeping all other parameters the same. This consistency provides further support for distal control of the geminate rebinding rates.

In spite of the sparsity of time points acquired in this study, the rates recovered are remarkably consistent with those reported in

prior studies. Further work is in progress to explore ligand dynamics in HbA over a broader range of times and at higher density, which should allow a more precise determination of the relative rates and a clearer indication whether the α subunit kinetics are better described with a four-state model.

Direct detection of the time-dependent A and B site populations and their locations provide incisive targets for assessing and validating room-temperature, atomistic MD simulations of ligand dynamics in HbA. The ability to investigate the relations between protein structure, function, and dynamics at near atomic resolution and on time scales down to 150 ps helps provide a rational basis for understanding how proteins achieve their targeted objectives with such remarkable efficiency and selectivity.

Acknowledgments

References

[1] M.F. Perutz, F.S. Mathews, J. Mol. Biol. 21 (1966) 199.
[2] Q.H. Gibson, Biochem. J. 71 (1959) 293.
[3] J. Hofrichter, J.H. Sommer, E.R. Henry, W.A. Eaton, Proc. Natl. Acad. Sci. USA 80 (1983) 2235.
[4] D.A. Chernoff, R.M. Hochstrasser, A.W. Steele, Proc. Natl. Acad. Sci. USA 77 (1980) 5606.
[5] J.W. Petrich, C. Poyart, J.L. Martin, Biochemistry 27 (1988) 4049.
[6] P.A. Anfinrud, C. Han, R.M. Hochstrasser, Proc. Natl. Acad. Sci. USA 86 (1989) 8387.
[7] M. Lim, T.A. Jackson, P.A. Anfinrud, J. Am. Chem. Soc. 126 (2004) 7946.
[8] S. Kim, J. Park, T. Lee, M. Lim, J. Phys. Chem. B 116 (2012) 6346.
[9] V. Srajer, T. Teng, T. Ursby, C. Pradervand, Z. Ren, S. Adachi, W. Schildkamp, D. Bourgeois, M. Wulff, K. Moffat, Science 274 (1996) 1726.
[10] F. Schotte, M. Lim, T.A. Jackson, A.V. Smirnov, J. Soman, J.S. Olson, G.N. Phillips Jr., M. Wulff, P.A. Anfinrud, Science 300 (2003) 1944.
[11] M. Cammarata, L. Eybert, F. Ewald, W. Reichenbach, M. Wulff, P. Anfinrud, F. Schotte, A. Plech, Q. Kong, M. Lorenc, B. Lindenau, J. Rabiger, S. Polachowski, Rev. Sci. Instrum. 80 (2009) 015101.
[12] M.F. Perutz, J. Cryst. Growth 2 (1968) 54.
[13] D. Bourgeois, Acta Crystallogr. D Biol. Crystallogr. 55 (1999) 1733.
[14] S. Arzt, J.W. Campbell, M.M. Harding, Q. Hao, J.R. Helliwell, J. Appl. Crystallogr. 32 (1999) 554.
[15] TheCCP4Team, Acta Crystallogr. D Biol. Crystallogr. 50 (1994) 760.
[16] T. Ursby, D. Bourgeois, Acta Crystallogr. A53 (1997) 564.
[17] F. Schotte, J. Soman, J.S. Olson, M. Wulff, P.A. Anfinrud, J. Struct. Biol. 147 (2004) 235.
[18] C. Savino, A.E. Miele, F. Draghi, K.A. Johnson, G. Sciara, M. Brunori, B. Vallone, Biopolymers 91 (2009) 1097.
[19] S. Adachi, S.Y. Park, J.R. Tame, Y. Shiro, N. Shibayama, Proc. Natl. Acad. Sci. USA 100 (2003) 7039.
[20] R.F. Tilton Jr., I.D. Kuntz Jr., G.A. Petsko, Biochemistry 23 (1984) 2849.
[21] V. Srajer, Z. Ren, T.Y. Teng, M. Schmidt, T. Ursby, D. Bourgeois, C. Pradervand, W. Schildkamp, M. Wulff, K. Moffat, Biochemistry 40 (2001) 13802.
[22] M. Schmidt, K. Nienhaus, R. Pahl, A. Krasselt, S. Anderson, F. Parak, G.U. Nienhaus, V. Srajer, Proc. Natl. Acad. Sci. USA 102 (2005) 11704.
[23] D. Bourgeois, B. Vallone, A. Arcovito, G. Sciara, F. Schotte, P.A. Anfinrud, M. Brunori, Proc. Natl. Acad. Sci. USA 103 (2006) 4924.
[24] I. Birukou, D.H. Maillett, A. Birukova, J.S. Olson, Biochemistry 50 (2011) 7361.
[25] M.F. Lucas, V. Guallar, Biophys. J. 102 (2012) 887.
[26] G. Hummer, F. Schotte, P.A. Anfinrud, Proc. Natl. Acad. Sci. USA 101 (2004) 15330.
[27] K. Nienhaus, J.S. Olson, S. Franzen, G.U. Nienhaus, J. Am. Chem. Soc. 127 (2005) 40.
[28] D. Vitkup, G.A. Petsko, M. Karplus, Nature Struct. Biol. 4 (1997) 202.
[29] I. Birukou, R.L. Schweers, J.S. Olson, J. Biol. Chem. 285 (2010) 8840.
[30] J.S. Olson, R.J. Rohlfs, Q.H. Gibson, J. Biol. Chem. 262 (1987) 12930.
[31] J. Hofrichter, E.R. Henry, J.H. Sommer, R. Deutsch, M. Ikeda-Saito, T. Yonetani, W.A. Eaton, Biochemistry 24 (1985) 2667.
[32] L.P. Murray, J. Hofrichter, E.R. Henry, M. Ikeda-Saito, K. Kitagishi, T. Yonetani, W.A. Eaton, Proc. Natl. Acad. Sci. USA 85 (1988) 2151.
[33] J.S. Philo, J.W. Lary, T.M. Schuster, J. Biol. Chem. 263 (1988) 682.
[34] A. Ansari, E.E. DiIorio, D.D. Dlott, H. Frauenfelder, I.E. Iben, P. Langer, H. Roder, T.B. Sauke, E. Shyamsunder, Biochemistry 25 (1986) 3139.
[35] R.E. Brantley Jr., S.J. Smerdon, A.J. Wilkinson, E.W. Singleton, J.S. Olson, J. Biol. Chem. 268 (1993) 6995.
[36] S.V. Lepeshkevich, J. Karpiuk, I.V. Sazanovich, B.M. Dzhagarov, Biochemistry 43 (2004) 1675.
[37] S.V. Lepeshkevich, M.V. Parkhats, Stepuro II, B.M. Dzhagarov, Biochim Biophys Acta 1794 (2009) 1823.
[38] M. Lim, T.A. Jackson, P.A. Anfinrud, Science 269 (1995) 962.
[39] S.Y. Park, T. Yokoyama, N. Shibayama, Y. Shiro, J.R. Tame, J. Mol. Biol. 360 (2006) 690.